JOURNAL OF MATERIALS SCIENCE **39** (2004) 2043–2051

Stress analysis in thermal barrier coatings subjected to long-term exposure in simulated turbine conditions

B. G. NAIR*[‡], J. P. SINGH[‡], M. GRIMSDITCH[§]
[‡]*Energy Technology Division and* [§]*Materials Science Division, Argonne National Laboratory, Argonne, IL 60439, USA*
E-mail: jpsingh@anl.gov

In recent years, ruby fluorescence spectroscopy has been demonstrated as a powerful technique for monitoring residual stress evolution in the thermally grown oxide scale in thermal barrier coating (TBC) systems. The measured residual stresses, in turn, can be used to monitor evolution of damage in the coatings. Effective use of this technology for real-time damage monitoring requires the identification of trends in measured stresses that can be used as indicators of damage evolution. The present work focuses on studying the evolution of residual stresses in TBC systems during long-term exposure to turbine operating conditions. The coatings are electron beam physical vapor deposited (EBPVD) and atmospheric plasma sprayed (APS) zirconia. The stress evolution in both EBPVD and APS coatings is analytically modeled by an approach that takes into consideration contributions due to both thermal mismatch and oxide growth. Microstructural changes in the TBC system are correlated with measured stress trends through comparison with the modeled stresses. The stress measurements and modeling provide insight into failure modes and mechanisms, and to identify critical features in the measured stress data that can be used as indicators of failure in TBCs.

1. Introduction

Nickel-based superalloys with zirconia thermal barrier coatings (TBCs) have been identified as candidate materials for applications in turbines and engines. These materials would allow 100–200°C higher operating temperatures and thereby increase energy efficiency. Significant progress has been made over the last two decades on coating development [1–4] through techniques such as electron beam physical vapor deposition (EBPVD) and atmospheric plasma spraying (APS), and gains have been made on understanding the failure modes and mechanisms in TBC systems [5–10].

One critical need that still must be addressed for the commercialization of this technology is nondestructive damage-monitoring techniques that recognize symptoms of impending failure in TBC systems and thus prevent catastrophic failure. It is well recognized that residual stresses are induced in TBCs because of thermal mismatch between the ceramic top coat and the bond coat (a metallurgical coating)/substrate, and also because of oxidation of the bond coat layer. Transient thermal stresses induced during service are superimposed onto these residual stresses, and the combined stress state constitutes the driving force for crack initiation and growth, leading to eventual failure of TBC systems.

During service, a thermally grown oxide (TGO) layer, usually alumina, appears between the zirconia top coat and the metallic bond coat. The magnitude of the residual stress in the TGO can be an indicator of the overall state of stress in the coating system and can provide critical information on damage/microcracking. Because ruby fluorescence spectroscopy is a powerful tool for measuring residual stresses in alumina, in recent years a substantial volume of work has been done by a number of different groups in applying this technique to thermally grown alumina scales in TBC systems [11–13]. The goal of this body of work has been to develop ruby fluorescence spectroscopy as a nondestructive evaluation (NDE) technique to predict coating failure. Work has also been done in developing phenomenological models for TBC failure and in understanding the role of the thermally grown oxide layer in damage initiation and evolution [14–16]. However, there is a need to identify critical features in the stress distribution that can be used as reliable indicators of initiation and growth of damage in the coating system. Further, there is a need to develop models for interpreting trends in measured oxide stress and for correlating these trends with microstructural evolution of the TBC system.

This paper describes (1) the measurement of stresses in APS and EBPVD TBCs on cylindrical components subjected to long-term exposure in simulated turbine conditions and (2) analysis of the measured residual

---

Present address: Ceramatec Inc., Salt Lake City, UT, USA.

0022–2461 © *2004 Kluwer Academic Publishers*

stress data. The latter employed a simplified model that accounts for not only thermal mismatch and stresses introduced due to volume expansion during oxidation, but also the change in elastic modulus of the top coat by microcracking introduced during thermal exposure.

2. Materials and methods

The specimens used in this study included EBPVD and APS yttria-stabilized zirconia TBC systems (obtained from Siemens-Westinghouse Power Corp., Orlando, FL). The as-processed coatings consisted of a zirconia top coat layer, plasma-sprayed bond coat layer at low pressure, and a superalloy substrate, as shown in Fig. 1. The top coat and bond coat form concentric layers on a cylindrical superalloy rod of 8-mm diameter. The thickness of the zirconia top coat layers ranged from 300–400 μm, and the thickness of the bond coat layer was $\approx$150 μm. As seen in Fig. 1, the microstructure of the EBPVD coating is characterized by long columnar grains perpendicular to the top coat/bond coat interface. The bond coat in EBPVD TBC specimens was polished down to reduce surface roughness before deposition of the zirconia coating (this is a prerequisite for the evolution of such a columnar microstructure). The microstructure of the APS specimens is characterized by splats flattened with respect to the surface of the substrate. The TBC specimens were subjected to simulated thermal service conditions for various exposure times (nominally 242, 1000, 2500, 4500, 7000, and 16,000 h). The APS specimens failed between 6000 and 7000 h, whereas the EBPVD specimens were still intact after 16,000 h. The experimental conditions including the test temperature and the thermal cycling profile were similar to what would be expected during elevated temperature application in turbines. The specific experimental details of these thermal cycling tests are considered proprietary information to Siemens-Westinghouse Power Corporation. The elastic modulus of the zirconia top coat of the APS specimens was measured by a microindentation technique [9, 17, 18].

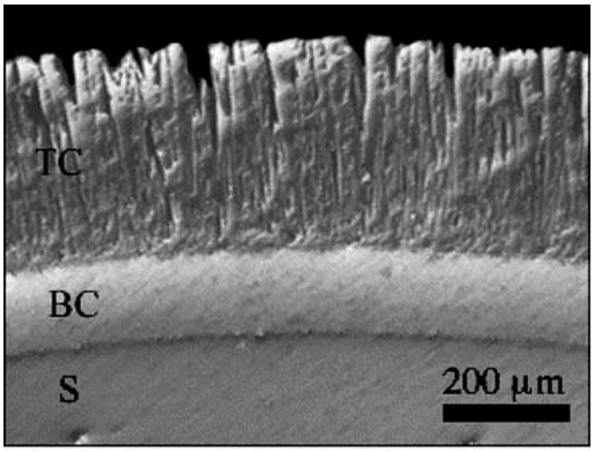

(a)

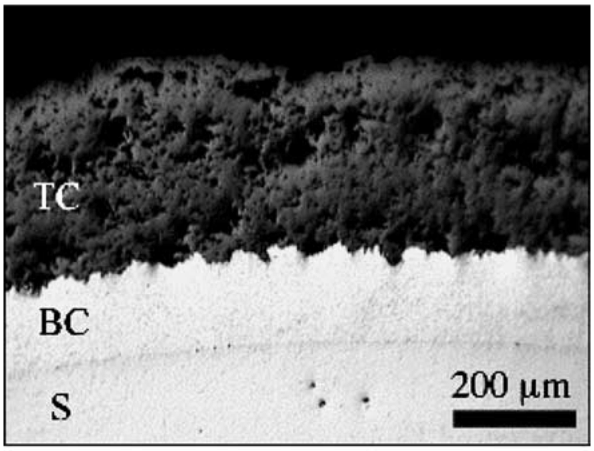

(b)

Figure 1 Microstructures of as-processed thermal barrier coatings applied by (a) EBPVD and (b) APS.

Residual stresses at the polished cross section of both EBPVD and APS TBC specimens were studied by ruby fluorescence spectroscopy. The spectra were excited with 50–100 mW of 476-nm radiation from a krypton ion laser and analyzed with a triple Jobin-Yvon grating spectrometer equipped with a charge-coupled device (CCD) detector (Princeton Instruments). Resulting spectra were recorded in both macro- and micro-configurations. In the macro experiments, the incident beam was focused down to a relatively broad circular spot size ($\approx$75 μm in diameter), and the scattered light was collected along the surface normal with an f/1.4 lens. The macro measurements on the polished cross section provide information about mean stresses in a given length (i.e., 75 μm) of the scale encompassed by the laser spot. For each specimen, eight macro measurements were made along the circumference of the oxide scale, and an average value was calculated. The micro spectra were acquired in the back-scattering mode through a microscope that allowed the laser to be focused to $\approx$2 μm. Because the beam size in the micro-mode was usually less than the scale thickness, the micro-mode measurements provide information on local stress states within the oxide scale.

The spectral data were collected with commercially available data acquisition software. Light from a standard krypton lamp was also directed to the detector to provide a reference peak for accurate calibration of the ruby peak shifts. A curve-fitting program, developed at Argonne National Laboratory, was used to accurately determine the peaks for a series of spectra. The peak shifts were calculated relative to reference peak spectra from stress-free alumina. The reference peak was estimated as an average value (694.28 $\pm$ 0.02 nm) obtained from stress-free single-crystal ruby and sapphire. It is well known that Cr_2O_3 content in Al_2O_3 results in a significant peak shift [19]. Therefore the reliability of the standard was verified by comparing it with data obtained from oxide scales spalled from superalloy substrates. The standard was found to be accurate within limits of experimental error.

It has been reported that the TGO layer on a NiCrAlY-bond coat typically has a columnar structure, with the columns oriented normal to the top coat/bond coat interface [20]. If we assume that the crystallites within these columns are randomly oriented, the frequency shift ($\bar{\Delta}\nu$) of the primary peak in the ruby spectra is related to the lattice strain. The elastic strain in the lattice can be correlated to the stress, and the residual stress tensor can be described by the general equation [21]:

$$\bar{\Delta}\nu = (1/3)\,\pi_{\text{ii}}\,\sigma_{\text{jj}} \qquad (1)$$

where σ_{jj} are the normal stresses in any arbitrary frame of reference, and π_{ii} are the corresponding piezospectroscopic coefficients. The frequency shift is not affected by shear stresses in the oxide scale. The triaxial stress state in the oxide scale of plasma sprayed coatings dictates that $\bar{\Delta}\nu$ is correlated to the principal stresses ($\sigma_{11}, \sigma_{22}, \sigma_{33}$) at each location in the scale as

$$\bar{\Delta}\nu = \left(\frac{\pi_{11}+\pi_{22}+\pi_{33}}{3}\right)(\sigma_{11}+\sigma_{22}+\sigma_{33}) \qquad (2)$$

The sum of stresses within the parentheses in Equation 2 is invariant, that is, $\sigma_{11}+\sigma_{22}+\sigma_{33} = \sigma_{\text{xx}}+\sigma_{\text{yy}}+\sigma_{\text{zz}} = 3\sigma_{\text{hyd}}$, where σ_{hyd} is the hydrostatic stress in the scale. The usually accepted range of ($\pi_{11} + \pi_{22} + \pi_{33}$) in Equation 2 is 7.52–7.61 cm^{-1}/GPa. In this manuscript, a value of 7.53 cm^{-1}/GPa is used, based on our calibration [22]. It should be noted here that the stress in the scale is probably not uniform. This non-uniformity seems to result in a broadening of the primary peak, as opposed to many sharp, narrow peaks. In our experiments, the maximum of this broad peak was used for frequency shift calculations, which would correspond to a mean stress in the oxide scale.

3. Results and discussion

For EBPVD specimens, the mean residual stress obtained from macro-ruby measurements as a function of exposure time is shown in Fig. 2. Initially, the magnitude of the mean compressive residual stress decreases sharply from ≈1.80 ± 0.32 GPa at 242 h to ≈1.38 ± 0.15 GPa after 1000 h. At higher exposure times, no significant change occurs in the measured mean residual stress. Further, the measured stresses in the EBPVD specimen are fairly uniform throughout the circumference of the oxide scale. This uniformity is expected in EBPVD specimens because the top coat/bond coat interface is relatively smooth, and local variations are minimized.

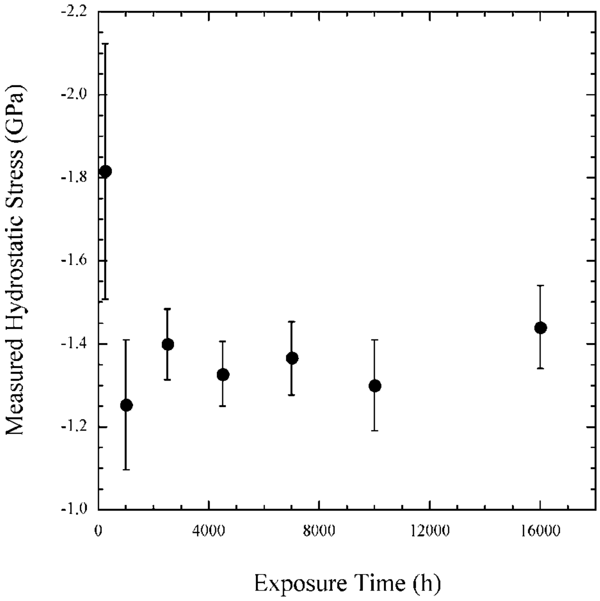

Figure 2 Variation of mean residual stress with exposure time in TGO of EBPVD TBCs subjected to simulated service environment.

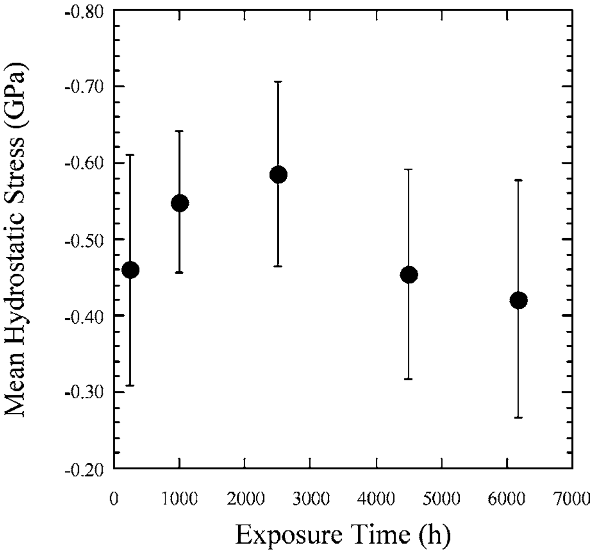

Figure 3 Variation of measured residual stress with exposure time in TGO of APS TBCs subjected to service environment.

The variation of measured residual stresses in the TGO layer of APS TBCs as a function of thermal exposure time is shown in Fig. 3; the measured compressive stress increases from ≈0.45 GPa at 242 h to ≈0.6 GPa at 2500 h of thermal exposure. After 2500 h, however, the residual stress decreased steadily to ≈0.42 GPa in the specimen that failed after 6158 h of thermal exposure.

To understand the observed trends in the variation of the measured stresses in EBPVD and APS TBC specimens with thermal exposure time, one must understand the role that the nature of the interface plays on local stress evolution in TBCs. Fig. 4 illustrates the correlation between the bulk geometry of the specimen and the specific microstructures shown in Fig. 1. For EBPVD specimens, where the interface is relatively smooth, an in-plane biaxial state of stress prevails in the TGO [21]. The primary stresses in the TGO of EBPVD specimens are σ_{R}, σ_{T}, and σ_{z}, as shown in Fig. 4. At the polished surface where the stresses are measured, the out-of-plane stress, σ_{z}, is relaxed, and its magnitude is expected to be low in relation to the in-plane thermal stress.

Hsueh rigorously analyzed the thermal mismatch stresses generated in concentric cylinders [23]. A calculation based on Hsueh's analysis for our bulk cylindrical EBPVD TBC specimens with and without the zirconia top showed that this coat has virtually no effect on thermal-mismatch-induced hydrostatic stress in the TGO. The calculated magnitude of the compressive hydrostatic stress in the TGO from thermal mismatch alone is ≈1.7 GPa, in good agreement with the stress after 242 h of exposure (≈1.8 GPa). This stress is significantly different from the steady-state stress observed after 1000 h (≈1.38 GPa). This observation clearly

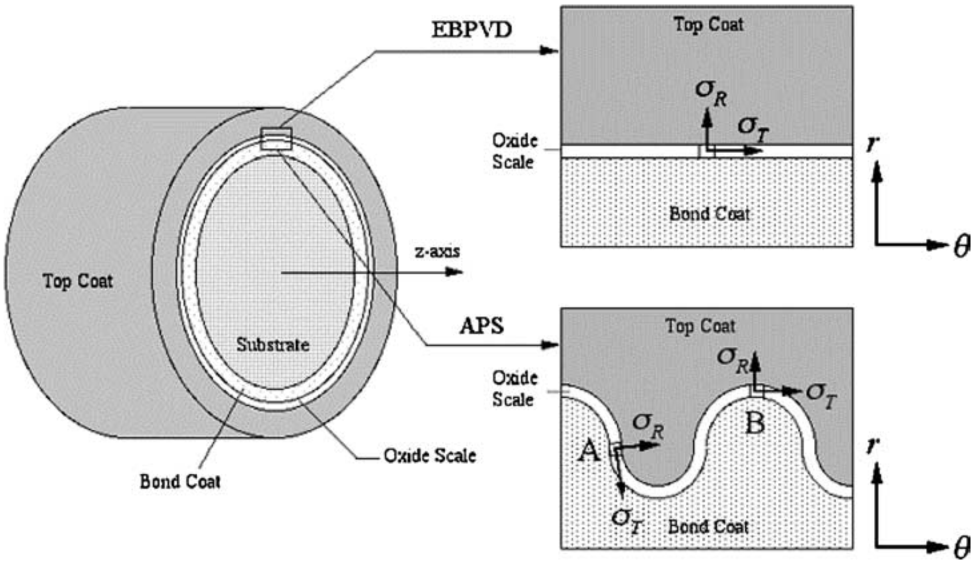

Figure 4 Schematic of bulk specimen with expanded cross sections of EBPVD and APS coatings. Drawing is not to scale. The rough interface of the APS coating results in the components of stress σ_T and σ_R being strong functions of the local interface geometry. In the EBPVD coatings, however, due to the relatively flat nature of the interface, σ_T and σ_R are nearly constant throughout the specimen. At the free surface, σ_z is expected to be very low due to stress relaxation.

suggests a relaxation of thermal mismatch stress in the TGO at longer exposure times (>242 h).

One possible cause for such relaxation is initiation and growth of microcracks in the TGO, which would reduce the effective elastic modulus. Although the TGO is under significant compressive stress, the generation of a randomly oriented crack structure can lead to the lowering of the elastic modulus. Scanning electron microscopy (SEM) of the TGO indeed showed significant microcracking after thermal exposure, as shown in Fig. 5. The elastic modulus of a material is an inverse function of microcrack size and density [24, 25]. As microcrack size and density increase, the elastic modulus decreases and approaches an asymptotic value. It is expected that with increasing exposure time, crack size and density will increase. Therefore, the elastic modulus of the oxide scale is expected to decrease and approach an asymptotic value during thermal exposure. Measured stress data suggest that the elastic modulus attains a steady-state value after about 1000 h of thermal exposure.

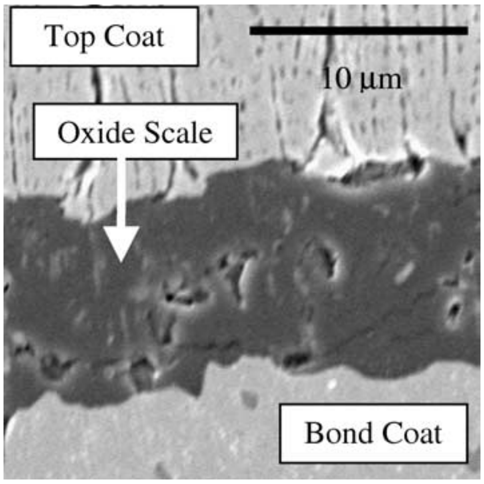

Figure 5 SEM photomicrograph of TGO in EBPVD TBC specimen subjected to 16,000 h of thermal exposure, showing extensive microcracking in oxide scale.

One can relate the variation of elastic modulus of the oxide scale, E_2 (the subscript 2 represents the oxide scale), with time as:

$$E_2 = E_{2,0} - C_{\mathrm{ox,m,1}}\left(1 - e^{-C_{\mathrm{ox,m,2}}t}\right). \tag{3}$$

In Equation 3, an exponential relationship for describing the time dependence of microcrack density is assumed for simplicity. $E_{2,0}$ is the initial elastic modulus of the Al_2O_3 scale (380 GPa), $C_{\mathrm{ox,m,1}}$ is the maximum relaxation in elastic modulus due to microcracking (taken to be 38 GPa, 10% reduction), and $C_{\mathrm{ox,m,2}}$ is a constant related to how fast the elastic modulus reaches its asymptotic value. If most of the relaxation (99%) occurs by 1000 h of exposure, $C_{\mathrm{ox,m,2}}$ would be 4.6×10^{-3} h^{-1}. Based on Hsueh's concentric cylinder model [23], an analysis was performed to estimate the residual stress in the bulk EBPVD TBCs, with the coating, oxide scale, and substrate/bond coat forming three concentric cylinders as illustrated in Fig. 4. Fig. 6 shows the modeled thermal stress in the EBPVD specimen for concentric cylinders, assuming a time-dependence for E_2 as noted in Equation 3. The model fits the data well, and the observed steady-state regime is due to the elastic modulus having reached its asymptotic value.

The apparent attainment of a steady-state stress explains the excellent thermal stability in EBPVD coatings. Eventual failure in EBPVD coatings is known to occur because of exaggerated oxide scale growth at surface flaws of the bond coat/oxide scale interface, and because of the associated stress concentrations at and near such flaws [26]. It is expected that the measured compressive hydrostatic stress in the oxide scale will decrease sharply as a crack initiates and grows at the interface, leading to failure. Evidence of this decrease was obtained through micro-ruby studies of local stresses around cracks in the oxide scale. Fig. 7a shows

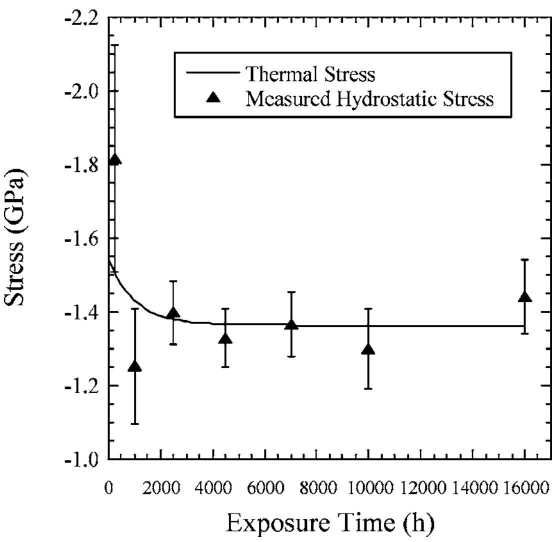

Figure 6 Variation of hydrostatic stress in oxide scale of EBPVD TBC systems predicted by the concentric cylinder model. The elastic modulus of oxide scale, E_2, is assumed to be a function of exposure time due to microcracking induced in oxide layer during thermal cycling.

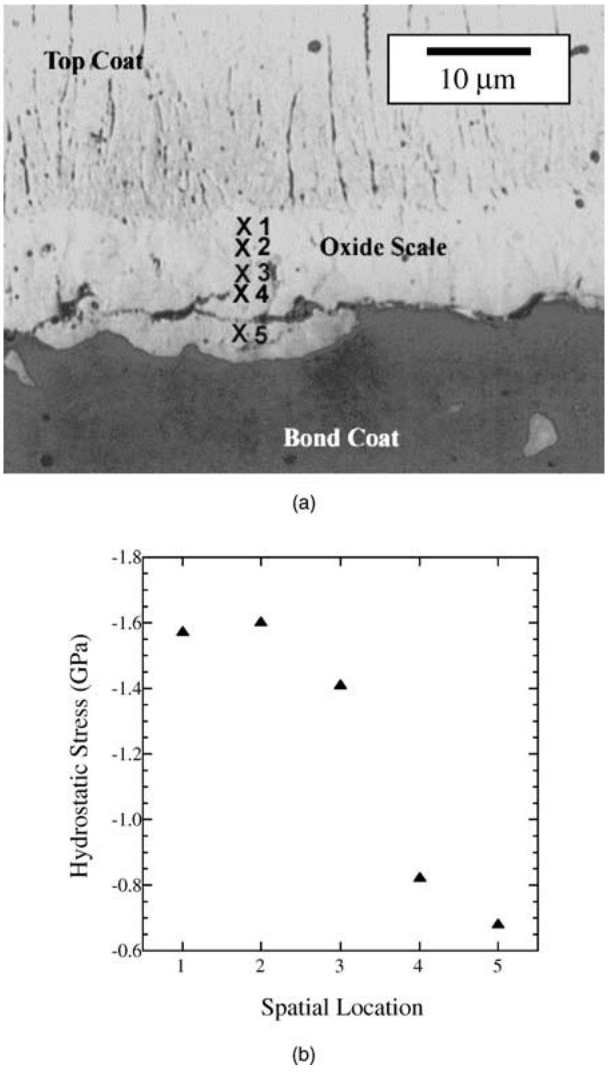

(a)

(b)

Figure 7 Evidence of stress relaxation in oxide scale adjacent to a large crack: (a) optical photomicrograph showing oxide scale in EBPVD TBC subjected to 16,000 h of accelerated thermal exposure indicating locations (marked by '×' and corresponding number) where micro-ruby stress measurements were made; (b) measured hydrostatic stresses at corresponding locations indicated in (a).

an optical photomicrograph of a crack in the oxide scale of an EBPVD specimen subjected to 16,000 h of accelerated thermal exposure. Each location at which ruby stress measurement were carried out is indicated by an '×' and a corresponding number in the photomicrograph. The stresses measured at each location in Fig. 7a are shown in Fig. 7b. Clearly, the stress in the regions adjacent to the crack is significantly relieved. Therefore, as the crack propagates in the oxide scale and the coating approaches failure, a significant decrease can be expected in the overall stress level, as measured by macro-ruby spectroscopy. Indeed, because such a reduction in the overall stress level can be an indicator of imminent failure, ruby fluorescence spectroscopy has great potential for nondestructive monitoring of damage in TBCs.

Clarke *et al.* [27] and Cheng *et al.* [28] reported stress values of ≈3–4 GPa in EBPVD TBCs, but the values reported in our study are lower for two reasons. First, in the current study the stresses were measured at the polished edge of a coating system, whereas in the above-noted studies, the measurements were made through the ceramic top coat. Because the out-of-plane stress (i.e., σ_z in Fig. 4) is relaxed at the polished edge, the measured stress is expected to be lower than that through the ceramic top coat. Indeed, this difference in measured stresses has been experimentally demonstrated in the same specimen by Singh *et al.* [29]. The second reason for the apparent discrepancy is that the reported values in Refs. 27 and 28 are for in-plane biaxial stress [i.e., $\sigma_{2,\text{biaxial}} = (\sigma_T + \sigma_z)/2$ in Fig. 4], whereas our data represent hydrostatic stress [i.e., $\sigma_{2,\text{hyd}} = (\sigma_R + \sigma_T + \sigma_z)/3$ in Fig. 4]. Because the out-of-plane stress, σ_R, is expected to be very low in comparison to in-plane stress, $(\sigma_R + \sigma_T + \sigma_z) \approx (\sigma_T + \sigma_z)$. Therefore, $\sigma_{2,\text{biaxial}} \approx 1.5\sigma_{2,\text{hyd}}$, and this difference causes a difference of ≈33% in reported stress value. In other words, our steady-state hydrostatic stress of 1.4 GPa corresponds to a biaxial stress of ≈2.1 GPa. Thus, considering the variations due to the geometry and the analysis employed, our values are actually in good agreement with the previously reported [27, 28] biaxial stress value of ≈3 to 4 Gpa.

In APS TBC specimens with wavy top-coat/bond-coat interfaces (unlike the case of the EBPVD specimen with flat interfaces), oxide growth plays an important role in residual stress evolution. Because of the wavy interface, oxide growth does not simply result in a translation of the top coat. Spectroscopic measurements and numerical modeling have demonstrated that this wavy geometry results in a nonzero stress component normal to the interface in TBCs [30, 31] and in free-standing oxide scales [32]. At certain locations within the protrusions of the top coat into the bond coat, the interface is perpendicular to the surface of the substrate. In such locations, growth of the TGO is constrained within a confined volume, and this condition can lead to significant compressive stresses due to oxidation-induced growth in the TGO.

The thermal mismatch stresses in plasma sprayed coatings with rough interfaces are expected to be lower than those measured in EBPVD coatings with relatively

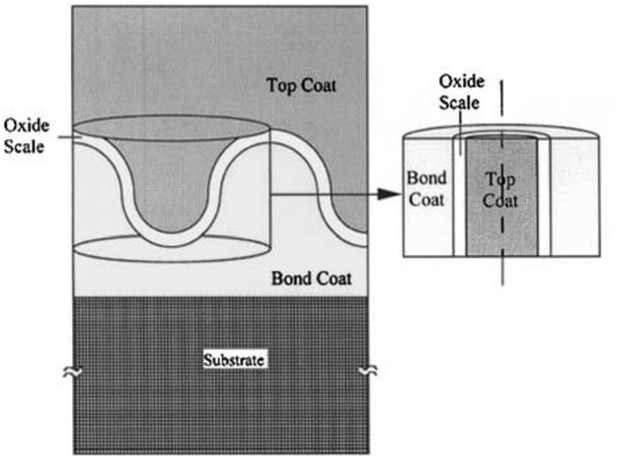

Figure 8 Geometry of concentric cylinder model used to investigate stresses at rough interface of APS TBC specimens.

flat interfaces. This effect is similar to that observed in oxide scales on superalloys where even a small extent of roughness significantly lowers the thermal-mismatch-induced stresses [33]. Indeed, the residual stresses reported here agree very well with those in similar plasma sprayed TBC systems [34, 35], and with those recent models that consider residual stresses due to oxide growth [36, 37].

The stress distribution in APS specimens, resulting from the combined effects of both oxide growth and thermal mismatch, is a strong function of the local interface geometry, and thus significant differences in local stresses are expected, depending on curvature and orientation of the interface [30]. A simplified analytical model is employed here to estimate the contribution of oxide-growth-induced stresses in APS TBCs. Each protrusion is considered to be a set of concentric cylinders (as illustrated in Fig. 8), similar to the approach used by Hsueh [23]. An analysis was performed using Hsueh's model with modified boundary conditions to calculate thermal mismatch stresses induced in protrusions of APS TBC specimens.

In addition to thermal-mismatch effects considered by Hsueh, stresses due to oxide growth within a constrained volume have also been considered in the present study. Oxide growth stresses result from a net increase in volume, as the high-density metallic bond coat is oxidized to form an oxide layer with a comparatively lower density. The change in volume is related to the molecular weights of the oxide and bond coat as

$$\beta = \frac{M_2\rho_3}{M_3\rho_2}, \tag{4}$$

where ρ_2 and ρ_3 are the densities, and M_2 and M_3 are the molecular weights, of the oxide scale and bond coat, respectively.

To better understand the generation of these stresses, oxide growth can be considered a three-stage process, as illustrated in Fig. 9, which shows the cross section of a protrusion in which the substrate, bond coat, and top coat are represented by concentric cylinders. In Stage I (prior to oxidation), the outer radii of the cylinders corresponding to the top coat and bond coat are a_0 and c_0, respectively. The top coat cylinder is removed temporarily as shown in Stage II, and oxidation of the bond coat is allowed to take place freely to form a scale so that no resulting stress occurs in any phase. Due to oxidation, the inner radius of the bond coat layer increases to b_0, and the inner and outer radii of the oxide scale become a_1 and b_0, respectively. At an arbitrary time, t, if the thickness of the oxide scale is d_0, then b_0 and a_1 can be expressed as

$$b_0 = a_0 + \frac{d_0}{\beta} \tag{5}$$

$$a_1 = b_0 - d_0. \tag{6}$$

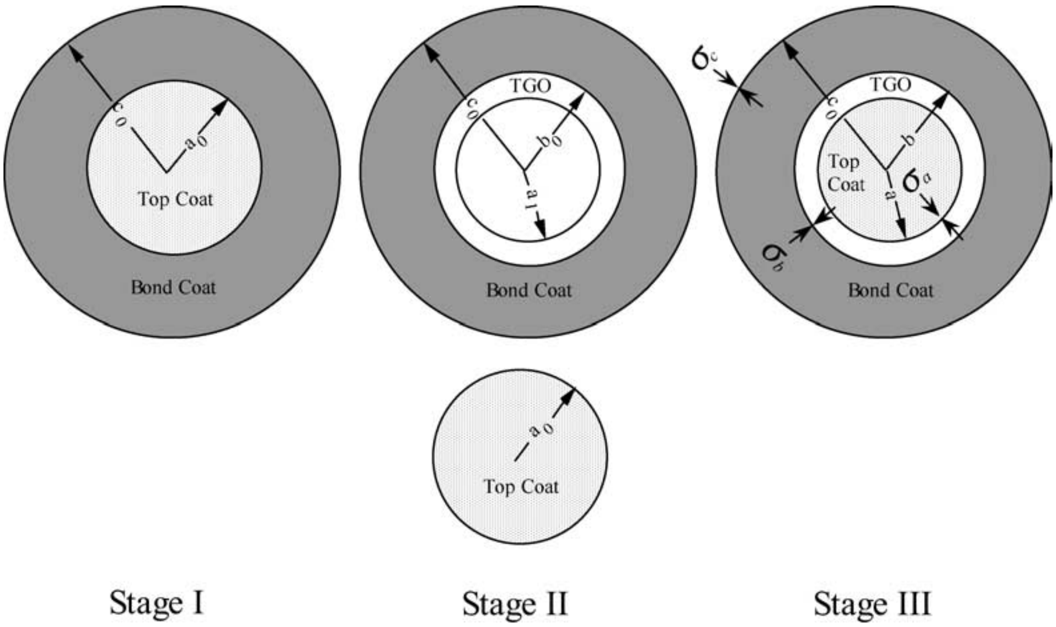

Figure 9 Stages of oxide growth within protrusions at rough interface of APS TBC specimens. Significant compressive growth stresses occur normal to interface within the TGO due to geometric constraints imposed on oxide growth and volumetric increase due to oxidation.

when the top coat is fitted back into the cavity, as shown in Stage III, the outer radii of the top coat and oxide layer change to a and b, respectively, to maintain displacement continuity. Because the protrusion under consideration is in contact with other similar protrusions at the rough interface, the outer radius c_0 does not change. This leads to the generation of normal stresses σ_a, σ_b, and σ_c at $r = a$, $r = b$, and $r = c_0$, respectively. Radial continuity conditions imposed on conventional thick cylinder equations [38, 39] can lead to the radial and tangential stresses in the three phases expressed in terms of σ_a, σ_b, and σ_c, as shown by

$$\sigma_{1,\mathrm{r}} = \sigma_\mathrm{a} \tag{7}$$

$$\sigma_{1,\mathrm{t}} = \sigma_\mathrm{a} \tag{8}$$

$$\sigma_{2,\mathrm{t}} = -\frac{a_1^2 b_0^2(\sigma_\mathrm{a} - \sigma_\mathrm{b})}{r^2\left(b_0^2 - a_1^2\right)} - \frac{\left(a_1^2\sigma_\mathrm{a} - b_0^2\sigma_\mathrm{b}\right)}{\left(b_0^2 - a_1^2\right)} \tag{9}$$

$$\sigma_{2,\mathrm{r}} = \frac{a_1^2 b_0^2(\sigma_\mathrm{a} - \sigma_\mathrm{b})}{r^2\left(b_0^2 - a_1^2\right)} - \frac{\left(a_1^2\sigma_\mathrm{a} - b_0^2\sigma_\mathrm{b}\right)}{\left(b_0^2 - a_1^2\right)} \tag{10}$$

$$\sigma_{3,\mathrm{t}} = -\frac{b_0^2 c_0^2(\sigma_\mathrm{a} - \sigma_\mathrm{b})}{r^2\left(c_0^2 - b_0^2\right)} - \frac{\left(b_0^2\sigma_\mathrm{b} - c_0^2\sigma_\mathrm{c}\right)}{\left(c_0^2 - b_0^2\right)} \tag{11}$$

$$\sigma_{3,\mathrm{r}} = \frac{b_0^2 c_0^2(\sigma_\mathrm{b} - \sigma_\mathrm{c})}{r^2\left(c_0^2 - b_0^2\right)} - \frac{\left(b_0^2\sigma_\mathrm{b} - c_0^2\sigma_\mathrm{c}\right)}{\left(c_0^2 - b_0^2\right)}, \tag{12}$$

where the subscripts 1, 2, and 3, represent the top coat, oxide scale, and bond coat, respectively. In these equations, $\sigma_{\mathrm{i,r}}$ and $\sigma_{\mathrm{i,t}}$ represent stresses in the radial and tangential directions in phase i. The tangential strains in the three phases, $\varepsilon_{\mathrm{i,t}}$, can be expressed as

$$\varepsilon_{\mathrm{i,t}} = \frac{\sigma_{\mathrm{i,t}} - \nu_\mathrm{i}\sigma_{\mathrm{i,r}}}{E_\mathrm{i}}. \tag{13}$$

From the geometry of the three phases, we can write the following equations by considering that the tangential strain at the interface is proportional to the change in the perimeter (which is proportional to the radius) of the interface:

$$\varepsilon_{1,\mathrm{t}} = \frac{a}{a_0} - 1 \quad \text{at } r = a_0 \tag{14}$$

$$\varepsilon_{2,\mathrm{t}} = \frac{a}{a_1} - 1 \quad \text{at } r = a_1 \tag{15}$$

$$\varepsilon_{2,\mathrm{t}} = \frac{b}{b_0} - 1 \quad \text{at } r = b_0 \tag{16}$$

$$\varepsilon_{3,\mathrm{t}} = \frac{b}{b_0} - 1 \quad \text{at } r = b_0 \tag{17}$$

$$\varepsilon_{3,\mathrm{t}} = 0 \quad \text{at } r = c_0. \tag{18}$$

Substituting from Equations 7–12 into Equation 13 and equating with Equations 14–18, we obtain a system of five equations and five variables $(a, b, \sigma_\mathrm{a}, \sigma_\mathrm{b}, \sigma_\mathrm{c})$ for an arbitrary value of d_0. From these equations, we can calculate σ_a and σ_b and use these to calculate the hydrostatic stress in the scale:

$$\sigma_{2,\mathrm{hyd}} = \frac{1}{3}(\sigma_{2,\mathrm{r}} + \sigma_{2,\mathrm{t}} + \sigma_{2,\mathrm{z}}) = -\frac{2\left(a_1^2\sigma_\mathrm{a} - b_0^2\sigma_\mathrm{b}\right)}{3\left(b_0^2 - a_1^2\right)} \tag{19}$$

An approximate solution for $\sigma_{2,\mathrm{hyd}}$, ignoring Poisson's effects for simplicity, can be written as

$$\sigma_{2,\mathrm{hyd}} \approx -\frac{2(a_0 - a_1)a_1^2 k_1\left[c_0^2(k_3 - 1) + b_0^2(k_3 + 1)\right]E_2}{3\left\{b_0^2(a_1k_1 + a_0)\left[b_0^2(k_3 - 1) + c_0^2(k_3 + 1)\right] + a_0a_1^2(k_3 - 1)\left(b_0^2 + c_0^2\right) - a_1^3k_1\left[b_0^2(k_3 + 1) + c_0^2(k_3 - 1)\right]\right\}} \tag{20}$$

where

$$k_1 = \frac{E_1}{E_2} \tag{21}$$

$$k_3 = \frac{E_3}{E_2}. \tag{22}$$

The system of equations was solved with numerical analysis software (Mathematica 4.0, Wolfram Research Inc., Champaign, IL) for exposure times ranging from 0.01 to 8000 h. Typical values were assumed for the properties of the top coat, oxide scale, and substrate, and for the dimensions of the protrusion for this calculation ($E_{1,0}$ = 100 GPa, $E_{2,0}$ = 380 GPa, E_3 = 200 GPa, $\nu_1 = 0.3$, $\nu_2 = 0.3$, $\nu_3 = 0.3$, $a_0 = 25$ μm, c_0 = 40 μm, where subscripts 1, 2, and 3 represent the top coat, oxide, and bond coat, respectively).

The elastic moduli of the top coat and the oxide scale are not expected to be constants during thermal exposure. The actual elastic modulus of the top coat is a function of the extent of porosity and microcracking in the top coat. Fig. 10 shows the variation of elastic modulus of the top coat with exposure time determined by microindentation measurements. During thermal exposure,

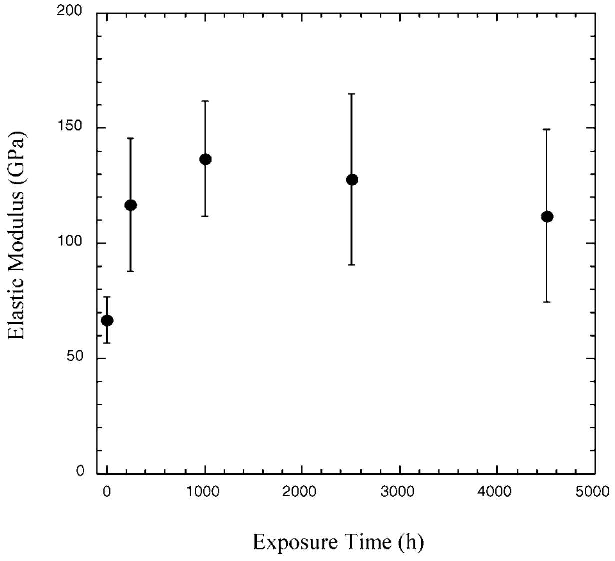

Figure 10 Variation of elastic modulus of zirconia top coat of APS TBC specimens measured by microindentation technique.

two processes occur in the top coat that affect the elastic modulus: (1) sintering of micropores within the top coat during the initial period of thermal exposure, resulting in increased elastic modulus; and (2) increase in microcracking within the top coat with increase in exposure time, resulting in decreased elastic modulus. The combined effect of these two processes results in an initial increase in elastic modulus when pore sintering dominates and an eventual decrease in elastic modulus due to the accumulation of microcracks [9]. Since pore sintering is a self-limiting thermally activated process, it is expected to have an exponential dependence on time. Due to the significantly higher thickness of the top coat compared to the oxide scale, the tangential stresses experienced by the top coat are lower. Therefore, because microcrack evolution is directly related to the stress level in the material, we can expect the rate of microcracking in the top coat to be lower than in the oxide scale. This results in the elastic modulus of the top coat approaching an asymptotic value only after a long time, assumed in our model to be 8000 h. Thus we can write

$$E_1 = E_{1,0} + C_{\mathrm{zir,s,1}}\left(1 - e^{-C_{\mathrm{zir,s,2}}t}\right) - C_{\mathrm{zir,m,1}}\left(1 - e^{-C_{\mathrm{zir,m,2}}t}\right), \qquad (23)$$

where $E_{1,0}$ is the elastic modulus of the top coat at time $t = 0$. $C_{\mathrm{zir,s,1}}$ and $C_{\mathrm{zir,m,1}}$ are constants that indicate the actual magnitude of the change in elastic modulus of the top coat due to sintering and microcracking, respectively. $C_{\mathrm{zir,s,2}}$ and $C_{\mathrm{zir,m,2}}$ are constants that determine how quickly the elastic modulus approaches its asymptotic value due to sintering and microcracking of the top coat, respectively. Based on the observed variation of the elastic modulus during thermal cycling of TBCs (Fig. 10), the values of the constants are assumed to be $E_{1,0} = 40$ GPa, $C_{\mathrm{zir,s,1}} = 20$ GPa, $C_{\mathrm{zir,s,2}} = 0.0015\mathrm{h}^{-1}$, $C_{\mathrm{zir,m,1}} = 60$ GPa, and $C_{\mathrm{zir,m,2}} = 400 \times 10^{-6}\ \mathrm{h}^{-1}$. Similarly, the elastic modulus of the oxide scale is expected to vary as indicated in Equation 3. Furthermore, the scale thickness has a parabolic dependence on time of exposure, as shown by

$$d_0 = k_{\mathrm{ox}}\, t^{1/2}, \qquad (24)$$

where $k_{\mathrm{ox}} = 0.095\ \mu\mathrm{m} \cdot \mathrm{h}^{-1/2}$, as calculated from scale thickness measurements on these specimens.

The time dependence of residual stress evolution in APS TBCs was determined by incorporating Equations 3, 23, and 24 into the concentric cylinder model described above. In Fig. 11, the residual thermal and oxide-growth stresses predicted by the model are shown separately as dashed and dotted lines, respectively. Initially, the oxide-growth stress increases due to the high initial growth rate associated with the parabolic nature of oxide growth. At longer exposure times, this rate decreases. Concurrently, elastic moduli of the top coat and oxide scale decrease due to accumulated TBC damage. The combined effect results in reduced residual stresses after long exposure times. The cumulative (thermal and oxide growth) residual stress predicted by the model is shown by the continuous line, which agrees very well with the measured stress data. Clearly, the excellent agreement of the model with the experimental data suggests that the residual stress in APS TBC specimens is influenced not only by thermal-mismatch stresses, but also by oxidation-induced stresses. The evolution of residual stress is influenced by microstructural evolution (specifically, sintering and microcracking) in the top coat and oxide scale.

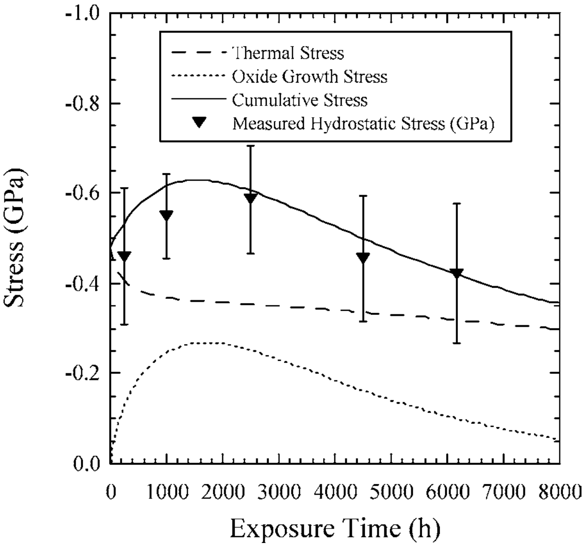

Figure 11 Variation of hydrostatic stress in oxide scale of protrusion in APS TBC systems predicted by concentric cylinder model. The elastic modulus of top coat, E_1, and elastic modulus of oxide scale, E_2, are assumed to be functions of exposure time.

4. Conclusions

Stress evolution in APS and EBPVD thermal barrier coatings subjected to accelerated thermal exposure in service environments was measured by ruby fluorescence spectroscopy. The EBPVD specimens survived after 16,000 h of exposure. Residual stress in the EBPVD coating was observed to drop to a steady-state value after ≈1000 h of thermal exposure and remain nearly constant after longer exposure times. Modeling the stresses in the EBPVD coating system by a concentric-cylinder model revealed that the observed stress distribution could be explained by the reduced elastic modulus of the oxide scale due to accumulation of damage (microcracking) with thermal exposure. Micro-ruby fluorescence spectroscopy indicated that as a failure crack propagates through the oxide scale, a significant drop in measured stress can be expected. Such a drop can be used as an indicator of failure initiation during nondestructive stress monitoring in a real-time service environment.

In APS TBC systems, the trend in stress data revealed an initial increase in measured stress up to 1500 h of exposure followed by a substantial decrease until the coatings fail at ≈6200 h of thermal exposure. The differences in observed trends in stress evolution between the EBPVD and APS specimens can be related to the nature of the top coat/bond coat interface. In EBPVD specimens, the interface is relatively flat, so growth of the oxide layer will result in a translation of the top coat. Therefore, oxide growth stresses do not contribute significantly to stress evolution in EBPVD systems, and the measured stresses are primarily due to thermal mismatch. However, the wavy interface in APS specimens characterized by protrusions of the interpenetrating layers can result in very high localized oxide growth stresses. Stress evolution in APS TBCs was modeled by considering each protrusion as a set of concentric cylinders. The elastic moduli of the top coat and of the oxide layer were assumed to be controlled by sintering and microcracking of the respective phases. The excellent agreement of the model with the experimental data suggests that the residual stress in APS TBC specimens is influenced not only by thermal mismatch stresses, but also by oxidation-induced stresses and microstructural changes in the top coat and oxide scale.

Acknowledgments

This work was supported by the U.S. Department of Energy, Office of Distributed Energy, under Contract W-31-109-Eng-38. The authors thank Dr. Stephen Sabol of Siemens-Westinghouse Power Corporation, Orlando, FL, for providing TBC specimens for this study and for helpful discussions.

References

1. T. E. STRANGMAN, E. D. FELTON and N. E. ULION, *Amer. Ceram. Soc. Bull.* **56**(8) (1977) 700.
2. S. M. GUPTA and D. K. GUPTA, *J. Engr. Gas Turb. Power* **111** (1989) 301.
3. T. M. YONUSHONIS, *J. Thermal Spray Tech.* **6**(1) (1997) 50.
4. Z. MUTASIM and W. BRENTNALL, *ibid.* **6**(1) (1997) 105.
5. R. D. MAIER, C. M. SCHEUERMANN and C. W. ANDREWS, *Amer. Ceram. Soc. Bull.* **60**(5) (1981) 555.
6. J. T. DEMASI-MARCIN, K. D. SHEFFLER and S. BOSE, *J. Engr. Gas Turb. Power* **112** (1990) 521.
7. B.-C. WU, E. CHANG, S.-F. CHANG and D. TU, *J. Amer. Ceram. Soc.* **72**(2) (1989) 212.
8. D. ZHU and R. A. MILLER, *Mater. Sci. Engr.* **A245** (1998) 212.
9. J. P. SINGH, M. SUTARIA and A. CHOPRA, *Ceram. Engr. Sci. Proc.* **19**(4) (1998) 313.
10. A. G. EVANS, D. R. MUMM, J. W. HUTCHINSON, G. H. MEIER and F. S. PETIT, *Prog. Mater. Sci.* **46**(5) (2001) 505.
11. X. PENG and D. R. CLARKE, *J. Amer. Ceram. Soc.* **83**(5) (2000) 1165.
12. A. SELCUK and A. ATKINSON, *Mater. Sci. Engr.* **A335** (2002) 147.
13. C.-H. HSUEH, J. A. HAYNES, M. J. LANCE, P. F. BECHER, M. K. FERBER, E. R. FULLER, JR., S. A. LANGER, W. C. CARTER and W. R. CANNON, *J. Amer. Ceram. Soc.* **82**(4) (1999) 1073.
14. K. W. SCHLICHTING, N. P. PADTURE, E. H. JORDAN and M. GELL, *Mater. Sci. Engr.* **A342** (2003) 120.
15. A. M. KARLSSON, J. W. HUTCHINSON and A. G. EVANS, *ibid.* **A351** (2003) 244.
16. X. CHEN, J. W. HUTCHINSON, M. Y. HE and A. G. EVANS, *Acta Mater.* **51** (2003) 2017.
17. D. B. MARSHALL, T. NOMA and A. G. EVANS, *Comm. Amer. Ceram. Soc.* **65**(10) (1982) C175.
18. J. P. SINGH, M. SUTARIA and M. FERBER, *Ceram. Engr. Sci. Proc.* **18**(4) (1997) 191.
19. Q. MA and D. R. CLARKE, *J. Amer. Ceram. Soc.* **76**(6) (1993) 1433.
20. J. A. HAYNES, M. K. FERBER, W. D. PORTER and E. D. RIGNEY, *Oxidation Met.* **52**(1/2) (1999) 31.
21. D. M. LIPKIN and D. R. CLARKE, *ibid.* **45**(3/4) (1996) 267.
22. D. RENUSCH, M. GRIMSDITCH, I. KOSHELEV, B. V. VEAL and P. Y. HOU, *ibid.* **48**(5/6) (1997) 471.
23. C.-H. HSUEH and E. R. FULLER, JR., *Scripta Mater.* **42** (2000) 781.
24. R. L. SALGANIK, *Izv. Akad. Nauk. SSSR. Mekh. Tverd. Tela.* **8**(4) (1973) 149.
25. D. P. H. HASSELMAN and J. P. SINGH, *Ceram. Bull.* **58**(9) (1979) 856.
26. M. GELL, K. VAIDYANATHAN, B. BARBER, J. CHENG and E. JORDAN, *Metall. Mater. Trans.* A **30A** (1999) 427.
27. D. R. CLARKE, R. J. CHRISTENSEN and V. TOLPYGO, *Surf. Coat. Tech.* **94/95** (1997) 89.
28. J. CHENG, E. H. JORDAN, B. BARBER and M. GELL, *Acta. Mater.* **46**(16) (1998) 5839.
29. J. P. SINGH, B. NAIR, D. RENUSCH, M. SUTARIA and M. GRIMSDITCH, *J. Amer. Ceram. Soc.* **84**(10) (2001) 2385.
30. B. G. NAIR, J. P. SINGH and M. GRIMSDITCH, *Ceram. Engr. Sci. Proc.* **21**(3) (2000), 133–141.
31. C.-H. HSUEH, J. A. HAYNES, M. J. LANCE, P. F. BECHER, M. K. FERBER, E. R. FULLER, JR., S. A. LANGER, W. C. CARTER and W. R. CANNON, *J. Amer. Ceram. Soc.* **82**(4) (1999) 1073.
32. J. K. WRIGHT, R. L. WILLIAMSON, D. RENUSCH, B. VEAL, M. GRIMSDITCH, P. Y. HOU and R. M. CANNON, *Mater. Sci. Engr.* **A262** (1999) 246.
33. S. URAN, B. W. VEAL, M. GRIMSDITCH, J. PEARSON and A. BERGER, *Oxidation Met.* **54**(1) (2000) 73.
34. M. J. LANCE, J. A. HAYNES, W. R. CANNON and M. K. FERBER, "Ceram. Trans. Nondestructive Evaluation of Ceramics," edited by C. H. Schilling and J. N. Gray (Amer. Ceram. Soc. Inc., Westerville, OH, 1998) vol. 89, p. 229.
35. K. W. SCHLICHTING, K. VAIDYANATHAN, Y. H. SOHN, E. H. JORDAN, M. GELL and N. P. PADTURE, *Mater. Sci. Engr.* **A291** (2000) 68.
36. A. M. LIMARGA, S. WIDJAJA, T. H. YIP and L. K. TEH, *Surf. Coat. Tech.* **153** (2002) 16.
37. K. SFAR, J. AKTAA and D. MUNZ, *Mater. Sci. Engr.* **A333** (2002) 351.
38. R. C. JUVINALL, in "Engineering Considerations of Stress, Strain and Strength," edited by K. H. Hill, McGraw-Hill, New York, (1967) p. 112.
39. C. H. HSUEH and E. R. FULLER, *Scripta Mater.* **42** (2000) 781.

Received 7 September
and accepted 6 November 2003